Air-Coupled Dynamic Behavior of Two-Dimensional Acoustic Sensors

Yuebin Zheng(郑跃滨)[1,2†], Zhaoyi Wan(万兆懿)[3†], Qin Zhou(周勤)[4†], Kaihui Liu(刘开辉)[5,3,2], Kehai Liu(刘科海)[1,2*], Chang Liu(刘畅)[3*], and Enge Wang(王恩哥)[3,1*]

[1]*Tsientang Institute for Advanced Study, Hangzhou 310024, China*
[2]*Songshan Lake Materials Laboratory, Institute of Physics, Chinese Academy of Sciences, Dongguan 523808, China*
[3]*International Centre for Quantum Materials, Collaborative Innovation Centre of Quantum Matter, Peking University, Beijing 100871, China*
[4]*Shanghai Yingxin Resonance Electromechanical Technology Co., Ltd., Shanghai 201800, China*
[5]*State Key Laboratory for Mesoscopic Physics, School of Physics, Peking University, Beijing 100871, China*

(Received 1 February 2026; accepted manuscript online 18 March 2026)

High-performance acoustic devices are essential to a wide array of modern technologies, including high-sensitivity detection electronics and industrial devices. In this context, two-dimensional (2D) materials emerge as highly promising candidates for next-generation acoustic sensing, owing to their exceptional properties. However, existing models, developed primarily for conventional thick membrane materials, are inadequate, as they neglect the significant air-coupled effects that dominate ultrathin 2D diaphragms. Here, we develop an equivalent lumped-element model (LEM) that effectively captures the air-coupled response of graphene diaphragms down to the monolayer thickness limit. This model demonstrates high accuracy, with a maximum deviation from experiment of approximately 2.8% ($\sim$0.24 dB) in the 100–20000 Hz range. By incorporating electrode radiation impedance, diffracted acoustic pressure, and viscous damping from backplate holes, this model enables precise optimization of 2D sensor performance. More broadly, this LEM framework can be extended to other ultrathin materials, establishing it as a general approach for modeling air-coupled dynamics in nanomaterial-based systems.

DOI: 10.1088/0256-307X/43/4/041001 CSTR: 32039.14.0256-307X.43.4.041001

Highly sensitive acoustic sensors have become vital in a broad spectrum of modern technologies, ranging from consumer electronics and healthcare[1–3] to industrial systems[4–6] and national defense.[7,8] To meet the growing demand for high-performance acoustic detection, acoustic sensors need to achieve high sensitivity, which intrinsically depends on the design of transducer diaphragms with large diameters and extreme thinness.[9] This configuration enhances the diaphragm's responsivity to weak pressure variations, thus improving the sensor's ability to detect low-amplitude signals.[10,11] However, conventional material diaphragms face fundamental limitations in achieving this configuration. One of the key bottlenecks is the severe degradation of their mechanical strength when fabricated into suspended structures with a large diameter-to-thickness ratio.[12] In this context, two-dimensional (2D) materials such as graphene provide the ideal properties of atomically thin geometry, exceptional mechanical strength, and ultra-low mass, thereby creating unprecedented opportunities for next-generation acoustic sensing platforms.[13,14]

Structurally, 2D material acoustic sensors can be categorized into unsuspended and suspended architectures. Unsuspended devices, which consist of a 2D material diaphragm on a thick substrate, such as artificial throats and eardrums[15–17] and humidity sensors,[18–20] offer straightforward fabrication and excellent stability. In the thick-film model, deformation is governed primarily by bending stiffness. This results in a displacement-dependent acoustic sensing mechanism, where the response is read out in real time by detecting the diaphragm displacement through voltage transduction.[21,22] However, the thick substrates (e.g., polyimide or polyethylene terephthalate films) with micrometer-scale thicknesses inherently restrict their sensitivity.[23]

In suspended architectures, the diaphragm is suspended without substrate support, thereby fully exhibiting the intrinsic properties of 2D materials, such as negligible bending stiffness and ultralow areal mass density (e.g., $\sim 1\times10^{-14}$ N·m and ~ 11 mg/m^2 for 5 nm-thick graphene, respectively).[24–26] This configuration with a thin diaphragm can support broadband frequency response.[27] The deformation behavior of the thin diaphragm is predominantly governed by built-in tension (also described as prestress). Given that the density of the 2D material diaphragm is comparable to the effective mass loading of the surrounding air (~ 10 mg/m^2),[28–30] the air-coupled effects cannot be neglected for the dynamic response and overall performance of 2D material sensors.[31,32]

To accurately predict the performance of 2D material acoustic sensors, dynamic models must incorporate air-coupled effects. However, conventional models are mainly

†These authors contributed equally to this work.
*Corresponding authors. Email: liu.chang@pku.edu.cn; khliu@tias.ac.cn; egwang@pku.edu.cn
© 2026 Chinese Physical Society and IOP Publishing Ltd. All rights, including for text and data mining, AI training, and similar technologies, are reserved.

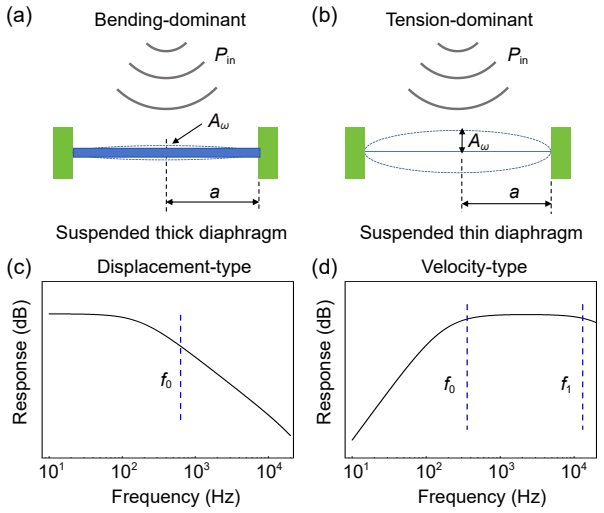

Fig. 1. Comparison of suspended architectures in 2D material acoustic sensors and their representative frequency responses. (a) Schematic of the suspended thick diaphragm configuration in the acoustic process, showing that the incident sound pressure $P_{\rm in}$ acts on the diaphragm. The diaphragm has radius a. The diaphragm's deflection A_ω is governed by thin-plate theory for relatively thick films, where bending stiffness dominates vibrational deformation. (b) Schematic of the suspended thin diaphragm configuration, made from 2D materials and governed by thin-membrane vibration theory, where prestress dominates deflection and damping effects are prominent. (c) Displacement-type frequency response of unsuspended devices, achieved using voltage transduction readout circuits, showing a stable operating bandwidth limited to sub-resonant frequencies below the fundamental resonance frequency f_0. (d) Velocity-type frequency response of suspended devices, achieved using current transduction readout circuits, exhibiting an extended flat bandwidth from the fundamental resonance frequency f_0 up to the high-frequency roll-off frequency f_1.

based on Wah theory,[33] which only focuses on the geometric and material parameters of the diaphragms. As a result, developing a new modeling approach that accounts for these critical air-coupled interactions becomes essential. Recently, an added virtual mass increment (AVMI) model has been proposed to explain the significant deviation between theoretical predictions and experimental measurements of the resonance frequency in graphene diaphragms.[13] Nonetheless, existing modeling methods, including AVMI, still exhibit limitations in computational time and predictive accuracy [Supplementary Materials (SM) Table S2].

In this work, we propose an equivalent lumped-element model (LEM) specifically for 2D material acoustic sensors. While the LEM has proven effective in capturing air-damping effects in high-fidelity microphones,[34,35] it was developed for stiffness-dominated conventional diaphragms, where such effects are negligible. By accounting for these critical air-coupled effects, our model achieves high predictive accuracy for the complete frequency response, as confirmed by experimental results.

First, the response behaviors of thick diaphragms [Fig. 1(a)] and thin diaphragms [Fig. 1(b)] were compared by applying a simple harmonic oscillator model. Thicker diaphragms are well-suited for designing displacement-type acoustic sensors using tailored voltage-based readout circuits. These circuits directly detect displacement-induced changes in capacitance arising from variations in electrode spacing. As illustrated in the normalized frequency response of a typical thick diaphragm [Fig. 1(c)], the operational bandwidth is restricted to frequencies below the fundamental resonance frequency f_0, with a sharp roll-off thereafter, thereby confining their utility to low-frequency regimes. In contrast, thinner diaphragms are more suitable for realizing velocity-type acoustic transduction using current-based readout circuits. These circuits directly measure the average velocity of the diaphragm, which is proportional to the incident acoustic pressure variation [Fig. 1(d)]. This design yields a flat frequency response from the fundamental resonance f_0 up to the high-frequency roll-off point f_1 [Fig. 1(d)], enabling broadband detection. Their relatively lower stiffness allows response to weak pressure perturbations, enhancing overall sensitivity (SM Note S1).

In order to accurately describe the acoustic sensor response, the LEM was developed in the thin diaphragm regime. The typical structure comprises a suspended 2D diaphragm positioned between two backplates. Incident waves cause the input sound pressure $P_{\rm in}$. Through diffraction, pressure waves propagate around the frame (with frame length $2L_{\rm F}$) and reach the diaphragm's backside, causing the diffracted pressure $P_{\rm D}$. The acoustic pressure radiated by the diaphragm's vibration is $P_{\rm R}$. While $P_{\rm D}$ and $P_{\rm R}$ are treated as controllable perturbations in traditional acoustic sensors, this approximation breaks down for 2D material sensors. FEM simulations provide reliable evidence for this breakdown (detailed in SM Note S3, Table S3, and Fig. S5a). The simulated sound velocity contours clearly illustrate that the net driving force on the diaphragm emerges from the complex interplay of incident, diffracted, and radiated waves (shown in SM Fig. S5b), confirming the significant contribution of air-coupled effects.

In the LEM framework, the acoustic processes of the system are represented using an electrical circuit analogy. Acoustic pressure is mapped to voltage, volume velocity (defined as the membrane velocity multiplied by the effective diaphragm area) to current, and acoustic impedance (pressure divided by volume velocity) to electrical impedance (voltage divided by current). Similar to this mapping, physical elements can be represented as electrical components. The damping element is represented by a resistor (R), the mass by an inductor (L), and the compliance element by a capacitor (C) (SM Fig. S4b). The incident sound force $P_{\rm in}S$ drives the circuit through the combined influence of the radiation impedance $Z_{\rm R}$, the characteristic impedance $Z_{\rm c}$, the diaphragm mechanical impedance $Z_{\rm m}$, and other circuit components. A symmetrical circuit topology is applied to account for the diffracted pressure $P_{\rm D}$, accurately describing the low-frequency air-coupled effects (detailed derivation is provided in SM Note S3).

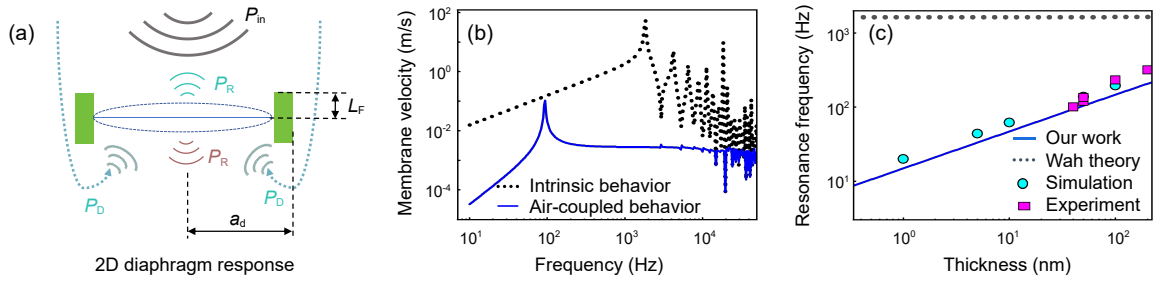

Fig. 2. Velocity-type frequency responses and comparative modeling analysis for graphene-based 2D material diaphragms. (a) Schematic of the acoustic response process in a 2D material acoustic sensor, showing incident sound pressure $P_{\rm in}$ diffracting around the rigid frame to generate diffracted sound pressure $P_{\rm D}$ on the diaphragm and outer frame. The diaphragm's vibration produces radiation pressure $P_{\rm R}$, illustrating air-coupling effects at low frequencies. The rigid frame has half-length $L_{\rm F}$, and the outer frame has radius $a_{\rm d}$. (b) Velocity-type frequency responses of the graphene diaphragm under vacuum (black dotted line) and air-coupled (blue solid line) conditions. The marked downward shift in resonance frequencies under air-coupled conditions arises primarily from the added mass effect due to acoustic radiation impedance. (c) Comparison of predicted and measured fundamental resonance frequencies (f_0) for graphene-based 2D material diaphragms with thicknesses ranging from 1 nm to 200 nm. Predictions are shown for the proposed LEM (blue solid line), Wah theory (gray dashed line), COMSOL simulations (cyan circles), and experimental data (pink rectangles). Wah theory substantially overestimates f_0 in the sub-200 nm regime owing to its neglect of air-coupled damping. In contrast, the LEM yields the closest agreement with both simulations and experiments, confirming its superior accuracy in capturing air-diaphragm interactions in ultrathin diaphragms.

Air-coupled effects impose a pressure modulation on the membrane vibration and velocity-type frequency response, generating an added mass $m_{\rm added}$ that significantly affects the diaphragm's fundamental resonant frequency, given by the following expression:[13]

$$f_{0n} = \frac{\alpha_{0n}}{2\pi a}\sqrt{\frac{T}{\mu + m_{\rm added}/S}}, \tag{1}$$

where n denotes the mode index, α_{0n} are Bessel zeros (e.g., 2.405 for $n = 1$), T is the diaphragm tension, a is the diaphragm radius, S is the effective area of the diaphragm, and μ is the areal mass density of the diaphragm. The added mass $m_{\rm added}$ effectively increases the total inertial load of the diaphragm, resulting in a pronounced downward shift in f_{01} [blue solid line in Fig. 2(b)] compared to the vacuum simulation [black dotted line in Fig. 2(b)]. Furthermore, the coupling effects from $P_{\rm D}$ and $P_{\rm R}$ effectively suppress the resonant peak and flatten the frequency response of the sensor [blue solid line in Fig. 2(b)]. These effects are further substantiated by experimental measurements [Fig. 2(c)]. Specifically, the fundamental resonant frequencies of graphene/graphite diaphragms with thicknesses spanning 1 nm to 200 nm are calculated using the LEM [blue solid line in Fig. 2(c)], Wah theory [gray dashed line in Fig. 2(c)], COMSOL FEM simulations [cyan circles in Fig. 2(c)], and directly compared to the experimental data [pink rectangles in Fig. 2(c); detailed parameters in SM Table S3]. These comprehensive comparisons clearly demonstrate that the LEM delivers the highest predictive accuracy across the entire thickness range. Notably, under identical conditions, the LEM not only delivers similar precision compared to FEM but does so in substantially reduced computational time (approximately seconds for LEM versus minutes for FEM).

To fully capture the complete structure of the 2D material-based acoustic sensor, the proposed LEM framework is extended and refined [Fig. 3(a)]. This further incorporates two perforated backplates with arrays of small holes (diameter $a_{\rm h}$) separated by air gaps of thickness g on each side. The hole dimensions are maintained much smaller than the operating acoustic wavelength to ensure the validity of the lumped-element approximations. The dual-backplate configuration is deliberately chosen to enable the diaphragm to operate in a highly linear regime while retaining exceptional sensitivity.[27] Conventionally, the small holes act as acoustic conduits. However, due to the significant air-related mutual coupling between adjacent holes, a more accurate description of the effective radiation impedance $Z_{\rm e}$ of the entire backplate is required. To quantify this behavior, we introduce a filling factor Γ to represent the fractional open area of the holes on each backplate. Viscous and thermal losses through the holes are fully incorporated into the comprehensive air-coupling framework. These dissipative effects profoundly influence both the back pressure $P_{\rm B}$ behind the diaphragm and the backplate radiation pressure $P_{\rm e}$ from the perforated backplates, ensuring an accurate and complete description of the 2D material sensor behavior (detailed in SM Note S4).

Integrating all the air-coupled interactions, we derive a complete equivalent LEM tailored for audio-frequency graphene-based acoustic sensors [Fig. 3(b), with the geometrical parameters detailed in SM Table S5]. To elucidate how these air-coupled effects modulate the real acoustic sensor response, we first examine the effective net driving force $\Delta F = S(P_{\rm in} - P_{\rm B})$ acting on the diaphragm [Fig. 4(a)]. Due to pronounced diffraction at low frequencies, the opposing back pressure $P_{\rm B}$ effectively counteracts the incident pressure $P_{\rm in}$, resulting in a markedly diminished real part of the effective driving force in the low-frequency regime [red dashed line in Fig. 4(a)]. Physically, this manifests as a drastic reduction in the net force on the diaphragm, which directly accounts for the characteristic

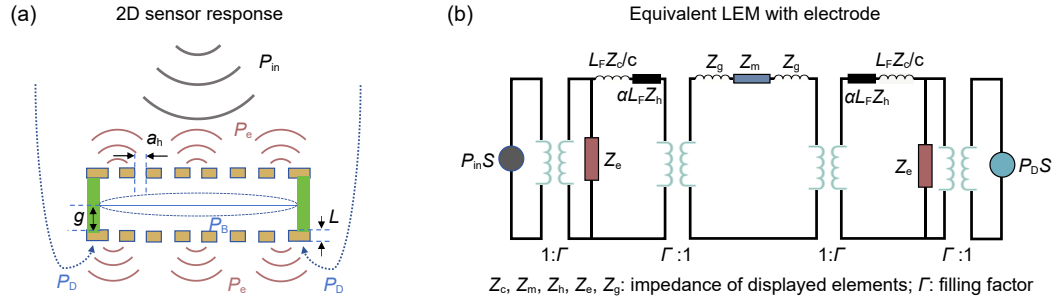

Fig. 3. Schematic of the 2D material-based acoustic sensor structure and its equivalent lumped-element models (LEMs). (a) Cross-sectional view of the sensor architecture. Incident acoustic pressure $P_{\rm in}$ arrives from the top, diffracts around the rigid frame to produce diffracted pressure $P_{\rm D}$, and drives diaphragm vibration to generate backplate radiated pressure $P_{\rm e}$ from the perforated back electrodes. The opposing pressure on the backside is $P_{\rm B}$. Key geometrical parameters include air gap thickness g, electrode thickness L, hole radius $a_{\rm h}$, and the membrane effective surface area S (with radius a). The perforated backplates feature arrays of small holes that facilitate acoustic transmission and damping. (b) Complete equivalent LEM incorporating perforated backplate effects. The circuit uses $P_{\rm in}S$ as the source, connected through $Z_{\rm c}$ (scaled by L/c) and a $1:\Gamma$ transformer (where Γ is the filling factor representing the open hole area fraction), then to hole impedance $Z_{\rm h}$ (scaled by $\alpha L/Z_{\rm h}$, with α as the attenuation coefficient), electrode radiation impedance $Z_{\rm e}$, and transformed impedance across the gap $Z_{\rm g}$, paralleled with $Z_{\rm m}$, and symmetrically mirrored on the backside leading to $P_{\rm D}S$. Additional transformers ($1:\Gamma$ and $\Gamma:1$) account for area discontinuities and mutual hole interactions.

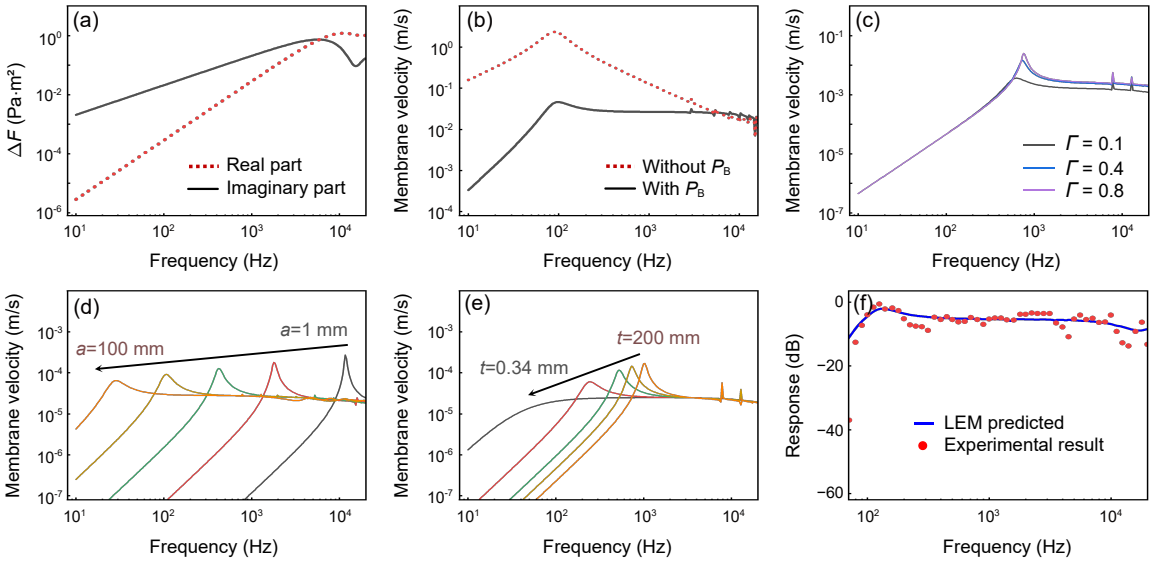

Fig. 4. Dynamic response characteristics, parameter optimization, and experimental validation of the equivalent LEM for graphene-based acoustic sensors. (a) Frequency dependence of the effective driving force on the diaphragm, decomposed into real (in-phase) and imaginary (quadrature) components. In the low-frequency regime, the markedly diminished real part reflects strong opposition from back pressure $P_{\rm B}$, resulting in reduced net drive and suppression of resonance peaks. (b) Velocity-frequency responses with (black solid line) and without (red dotted line) inclusion of back pressure $P_{\rm B}$, illustrating that $P_{\rm B}$ is essential for reproducing the characteristic low-frequency roll-off and flattened bandwidth observed in ultrathin diaphragms. (c) Velocity-frequency responses as a function of backplate filling factor Γ. Tuning Γ enables precise control of viscous and thermal damping, optimizing low-frequency response and resonance behavior. (d) Velocity-frequency responses for diaphragms of varying radius (diameters from 1 mm to 100 mm, at fixed thickness of 20 nm and $\Gamma = 0.4$) (calculated). Increasing radius shifts resonance peaks to lower frequencies, broadening and flattening the response. (e) Velocity-frequency responses for diaphragms of varying thickness (200 nm to 0.34 nm monolayer, at fixed diameter of 20 mm and $\Gamma = 0.4$). Decreasing thickness similarly lowers resonance frequencies while extending and flattening the bandwidth. The results of (a)–(e) were calculated using the proposed LEM framework. (f) Comparison of LEM-predicted (blue line; calculated) and experimentally measured (red dots) velocity-frequency responses for a fabricated graphite diaphragm sensor. The model shows excellent agreement across the audio range, with a maximum deviation of only $\sim 2.8\%$ (~ 0.24 dB).

roll-off and flattening of the sensor's frequency response at low frequencies. To demonstrate that this flattening of the frequency response stems directly from the back pressure $P_{\rm B}$, we compare model predictions with and without its inclusion [Fig. 4(b)]. The presence of $P_{\rm B}$ dramatically suppresses both the diaphragm's vibration velocity (membrane velocity) and the resonance peak amplitude [red dashed line in Fig. 4(b)]. In contrast, neglecting $P_{\rm B}$

produces an unrealistic upturn in the response, which contradicts the established behavior of 2D material acoustic sensors. This profound influence of P_B further emphasizes the necessity of incorporating air-coupling effects in accurate modeling of 2D material acoustic sensors.

More importantly, the LEM enables direct optimization of acoustic damping and losses that are challenging to precisely control in other models. By intuitively mapping these acoustic damping and loss mechanisms to specific elements in the electro–acoustic equivalent circuit, the model enables optimization not only through adjustments to geometric parameters (e.g., the backplate filling factor Γ), but also by directly assigning values to abstract impedance and damping components. By tuning the backplate filling factor [Fig. 4(c)], the damping mechanisms driven by viscous and thermal losses can be quantitatively controlled. A higher Γ (increased open area fraction) significantly amplifies fundamental vibration amplitudes, which can be designed for sensors targeting low-frequency performance. Conversely, a lower Γ enhances resonance damping, resulting in an extended flat bandwidth more suited for broadband acoustic sensing applications. Increasing the radius [Fig. 4(d)] or decreasing the thickness [Fig. 4(e)] shifts resonance peaks toward lower frequencies. It is notable that, for thinner membranes, air damping effectively suppresses higher-order resonance modes, leading to a smoother, flatter broadband response (Fig. S8 of the SM). At the monolayer limit (~ 0.34 nm), for example, a 20 mm diameter diaphragm under 1 MPa prestress can achieve a resonance frequency of ~ 6 Hz, yielding a simulated frequency response wider and flatter compared to those obtained with thicker diaphragms. Furthermore, the velocity-type frequency response predicted by the equivalent LEM is rigorously validated against experimental measurements [Fig. 4(f)]. The model achieves high agreement with the data, exhibiting a maximum deviation of only $\sim 2.8\%$ (~ 0.24 dB) across the 100–20000 Hz audio range.

Leveraging the LEM for design optimization, the fabricated device realizes an extraordinary diameter-to-thickness ratio approaching 10^6 (80 mm diameter and 100 nm thickness; Fig. S2b of the SM). This achieves a flat bandwidth exceeding 30 kHz, with the sensitivity approaching the highest values for capacitive acoustic sensors. These results demonstrate the practical utility of the LEM as a powerful tool for engineering high-performance acoustic sensors. The LEM can also be extended for high-frequency and large-radiation applications (Fig. S6b of the SM), making it suitable for aeroacoustic or ultrasonic transduction, such as micro-electro-mechanical systems (MEMS) and nano-electro-mechanical systems (NEMS) resonators.[36]

In conclusion, the developed equivalent LEM provides a highly accurate framework for modeling air-coupled dynamics in suspended 2D material acoustic sensors. By mapping physical quantities to specific elements in the electro–acoustic equivalent circuit, the LEM enables direct prediction and parameter control. This versatile framework holds substantial promise for extension to the vibration dynamics of other air-coupled nanostructures, offering valuable guidance and inspiration for future research and device engineering.

Acknowledgements. This work was supported by the Guangdong Major Project of Basic and Applied Basic Research (Grant No. 2021B0301030002), the New Cornerstone Science Foundation through the XPLORER PRIZE, the National Natural Science Foundation of China (Grant No. 12574185), Postdoctoral Science Foundation of China (Grant Nos. 2022M720629, 2025T180922, and 2022M710232), Hangzhou Tsientang Education Foundation, and Young Elite Scientists Sponsorship Program of the Beijing High Innovation Plan.

References

[1] Wang Y, Sun C, and Ahmed D 2025 *Nat. Electron.* **8** 485
[2] Chen Y, Liu H, Reilly M, Bae H, and Yu M 2014 *Nat. Commun.* **5** 5247
[3] Wu Z, Liu K, Wang Y, and Zheng Y 2015 *J. Intell. Mater. Syst. Struct.* **26** 2181
[4] Zheng Y, Liu K, Wu Z, Gao D, Gorgin R, Ma S, and Lei Z 2019 *Ultrasonics* **92** 13
[5] Basiri-Esfahani S, Armin A, Forstner S, and Bowen W P 2019 *Nat. Commun.* **10** 132
[6] Cheng X, Zhou X, Huang C, Liu C, Ma C J, Hong H, Yu W T, Liu K H, and Liu Z F 2021 *Chin. Phys. B* **30** 118103
[7] Kaushik B, Nance D, and Ahuja K 2005 *11th AIAA/CEAS Aeroacoustics Conference* 2005 Monterey, California, 2005-2997
[8] de Bree H E and Wind J W 2011 *Proc. SPIE* **8047** 80470C
[9] Wan Z Y, Liu H Z, Zheng Y B, Ma Y H, Liu K H, Zhou X, Liu C, Liu K H, and Wang E 2024 *Adv. Funct. Mater.* **34** 2303519
[10] Pan L, Chortos A, Yu G, Wang Y, Isaacson S, Allen R, Shi Y, Dauskardt R, and Bao Z 2014 *Nat. Commun.* **5** 3002
[11] Zhu J K, Wang L M, Wu J Q, Liang Y C, Xiao F, Xu B, Zhang Z J, Fan X L, Zhou Y, and Xia J 2023 *Chin. Phys. Lett.* **40** 038102
[12] Beranek L L and Mellow T J 2019 *Acoustics: Sound Fields, Transducers and Vibration* (Academic Press)
[13] Pezone R, Baglioni G, van Ruiten C, Anzinger S, Wasisto H S, Sarro P M, Steeneken P G, and Vollebregt S 2024 *Appl. Phys. Lett.* **124** 123503
[14] Yang Y B, Wang R Z, and Wang C H 2023 *Nanoscale* **15** 1860
[15] Dagdeviren C, Su Y, Joe P, Yona R, Liu Y, Kim Y S, Huang Y A, Damadoran A R, Xia J, Martin L W, Huang Y G, and Rogers J A 2014 *Nat. Commun.* **5** 4496
[16] Pozo-Bayón M Á, Santos M, Martïn-Álvarez P J, and Reineccius G A 2009 *Flavour Fragr. J.* **24** 226
[17] Yang J, Chen J, Su Y, Jing Q, Li Z, Yi F, Wen X, Wang Z, and Wang Z L 2015 *Adv. Mater.* **27** 1316
[18] Smith A D, Elgammal K, Niklaus F *et al.* 2015 *Nanoscale* **7** 19099
[19] Santra S, Hu G, Howe R C T, De Luca A, Ali S Z, Udrea F, Gardner J W, Ray S K, Guha P K, and Hasan T 2015 *Sci. Rep.* **5** 17374
[20] Bi H, Yin K, Xie X, Ji J, Wan S, Sun L T, Terrones M, and Dresselhaus M S 2013 *Sci. Rep.* **3** 2714
[21] Jabareen M and Eisenberger M 2001 *J. Sound Vib.* **240** 409

[22] Kirchhoff G 1850 *J. Reine Angew. Math.* **1850** 51
[23] Gou G Y, Li X S, Jian J M, Tian H, Wu F, Ren J, Geng X S, Xu J D, Qiao Y C, Yan Z Y, Dun G H, Ahn C W, Yang Y, and Ren T L 2022 *Sci. Adv.* **8** eabn2156
[24] Lee J U, Yoon D, and Cheong H 2012 *Nano Lett.* **12** 4444
[25] Gorgolis G and Galiotis C 2017 *2D Mater.* **4** 032001
[26] Lee J, Wang Z, He K, Shan J, and Feng P X L 2013 *ACS Nano* **7** 6086
[27] Zhou Q, Zheng J, Onishi S, Crommie M F, and Zettl A K 2015 *Proc. Natl. Acad. Sci. U.S.A.* **112** 8942
[28] Kinsler L E, Frey A R, Coppens A B, and Sanders J V 2000 *Fundamentals of Acoustics* (John Wiley & Sons)
[29] Li S and Li X 2008 *Appl. Acoust.* **69** 272
[30] Beranek L L and Mellow T J 2012 *Acoustics: Sound Fields and Transducers* (Academic Press)
[31] Nagaya K 1978 *J. Appl. Mech.* **45** 153
[32] Chiang H Y and Huang Y H 2018 *Appl. Acoust.* **129** 365
[33] Wah T 1962 *J. Acoust. Soc. Am.* **34** 275
[34] Liu H, Olson D A, and Yu M 2014 *J. Sound Vib.* **333** 7051
[35] Guan X 2025 *Sci. Rep.* **15** 27434
[36] Lin S C, Tian T, Yin P R, Huang P, Zhang L, and Du J F 2021 *Chin. Phys. Lett.* **38** 020502